Int. J. Electrochem. Sci., 15 **(2020)** 7493 – 7507, doi: 10.20964/2020.08.27

International Journal of
ELECTROCHEMICAL
SCIENCE
www.electrochemsci.org

Electrodeposition of Sn-Co-Ni and Sn-Co-Zn Alloy Coatings on Copper Substrate in a Deep Eutectic Solvent and Their Characterization

Tianyu Shi, Xingli Zou[*]*, Shujuan Wang, Zhongya Pang, Wei Tang, Guangshi Li, Qian Xu, Xionggang Lu*[*]

State Key Laboratory of Advanced Special Steel & Shanghai Key Laboratory of Advanced Ferrometallurgy & School of Materials Science and Engineering, Shanghai University, 99[#] Shangda Road, Shanghai 200444, China.
[*]E-mail: xlzou@shu.edu.cn (X. Zou); luxg@shu.edu.cn (X. Lu)

Received: 8 March 2020 / *Accepted:* 6 May 2020 / *Published:* 10 July 2020

Sn-Co-Ni and Sn-Co-Zn alloy coatings have been electrodeposited on Cu substrate from $SnCl_2$, $CoCl_2$, and $NiCl_2$ or $ZnCl_2$ precursors in choline chloride/urea (ChCl-urea) deep eutectic solvent (DES). Cyclic voltammetry experiments were applied to research the electrodeposition behaviors of Sn-Co, Sn-Co-Ni and Sn-Co-Zn alloy coatings in ChCl-urea ionic liquid. The results reveal that the reduction processes of Sn(II), Co(II), Ni(II) and Zn(II) are all one-step processes. The cathodic potential and electrodeposition time would influence the morphology of the Sn-Co, Sn-Co-Ni and Sn-Co-Zn alloy coatings significantly. With the increase of potential, the morphology of the deposited Sn-Co-Zn alloy coating changed from cubic crystals to flower-shaped particles, while the Sn-Co-Ni alloy coating varied from needle-like crystals to three-dimensional structure. The corrosion resistance of the Sn-Co-Ni and Sn-Co-Zn coatings electrodeposited at different potentials have also been researched and compared. It is suggested that the tin-based ternary alloy coatings with tunable microstructures can be directly and facilely electrodeposited in ChCl-urea electrolyte.

Keywords: Electrodeposition; Sn-Co-Ni alloy; Sn-Co-Zn alloy; Deep eutectic solvent; Corrosion

1. INTRODUCTION

Because of their excellent corrosion resistance, high chemical stability, and high power capacity [1-3], tin-based alloys have been widely used in electronics, machinery, industry and other fields [4, 5]. At present, the research of tin-based alloys by electrodeposition from aqueous electrolytes has been studied relatively well [6-9]. However, there are some disadvantages in electrodeposition in aqueous solutions, such as narrow electrochemical window, complex additives and environmental

concerns. Accordingly it is necessary to search for a suitable alternative for the tin-based alloys electrodeposition. Compared to aqueous solution, ionic liquids (ILs) have excellent characteristics, for instance, low vapor pressure, wide electrochemical window, good chemical, and thermostability [10-12]. In recent years, people have paid more and more attention to the electrodeposition in ionic liquids [13, 14]. Wang et al. [15] reported that SnCo alloys were electrodeposited from electrolyte composed of ionic liquid 1-ethyl-3-methylimidazolium chloride (EMIC), $SnCl_2$ and $CoCl_2$ without a template successfully. In addition, Sun et al. [16] have prepared CuSn alloy coating in 1-butyl-3-methylimidazolium chloride ([BMIM]Cl) using electrodeposition method. These studies suggest that electrodeposition of tin based alloy coatings from ILs is possible. However, the high costs and instability in air and moist condition of the imidazolium-based ILs would hamper their widely development [17, 18]. Therefore, it is necessary to find a cost-efficient and chemical and thermal stable ionic liquid for the electrodeposition of Sn-based alloys.

Deep eutectic solvents (DESs) are attached much attention at present. They are composed of quaternary ammonium salts and hydrogen bond donors in a certain proportion [19]. It has been demonstrated that the DESs provide promising opportunities for the electrodeposition processes [20, 21]. Actually, DESs have been recognized as environmentally friendly and low-cost ILs with excellent stability against air and moisture [22, 23]. Many researches have demonstrated that the electrodeposition of Sn and Sn-based binary alloys from DESs is feasible [24, 25]. However, there is rare systematical research on the electrodeposition of Sn-based ternary alloys such as Sn-Co-Ni and Sn-Co-Zn in DESs.

In this work, the electrodeposition of Sn-Co, Sn-Co-Ni and Sn-Co-Zn alloy coatings from $SnCl_2{\cdot}2H_2O$ (0.1M)-$CoCl_2{\cdot}6H_2O$ (0.04 M), $SnCl_2{\cdot}2H_2O$ (0.1 M)-$CoCl_2{\cdot}6H_2O$ (0.04 M)-$NiCl_2{\cdot}6H_2O$ (0.04 M) and $SnCl_2{\cdot}2H_2O$ (0.1 M)-$CoCl_2{\cdot}6H_2O$ (0.04 M)-$ZnCl_2$ (0.04 M) in ChCl-urea on Cu substrate has been systematically investigated. The influences of different cathodic potentials and electrodeposition times on the electrodeposition process and the morphology of the Sn-Co-Ni and Sn-Co-Zn ternary alloy coatings have been characterized in detail. Furthermore, the corrosion-resistance difference between the synthesized Sn-Co-Ni and Sn-Co-Zn alloy coatings has been compared, which may provide references for their applications.

2. EXPERIMENTAL

2.1 Electrolyte preparation

Choline chloride [$HOC_2H_4N(CH_3)_3Cl$] (ChCl) (Aldrich > 99%), and urea [NH_2CONH_2] (Aldrich > 99%) obtained from Sinopharm Chemical Reagent Co. Ltd, were dried at 353 K-363 K for about 5 h before use. $SnCl_2{\cdot}2H_2O$ (Aldrich > 99%), $CoCl_2{\cdot}6H_2O$ (Aldrich > 99%), $NiCl_2{\cdot}6H_2O$ (Aldrich > 99%) and $ZnCl_2$ (Aldrich > 99%) were also obtained from Sinopharm Chemical Reagent Co. Ltd. The DES was composed of the mixture (1:2 molar ratio) of ChCl and urea (12CU), which were mixed at 353 K for about 6 h until a steady and colorless liquid was obtained. The solution of 0.1 M $SnCl_2{\cdot}2H_2O$ and 0.04 M $CoCl_2{\cdot}6H_2O$, the solution of 0.1 M $SnCl_2{\cdot}2H_2O$, 0.04 M $CoCl_2{\cdot}6H_2O$ and

0.04 M $NiCl_2·6H_2O$ or the solution of 0.1 M $SnCl_2·2H_2O$, 0.04 M $CoCl_2·6H_2O$ and 0.04 M $ZnCl_2$ denoted as 12CU-$SnCl_2$ (0.1 M)-$CoCl_2$ (0.04 M), 12CU-$SnCl_2$ (0.1 M)-$CoCl_2$ (0.04 M)-$NiCl_2$ (0.04 M) and 12CU-$SnCl_2$ (0.1 M)-$CoCl_2$ (0.04 M)-$ZnCl_2$ (0.04 M), was added into the 12CU and stirred at 353 K for approximately 4 h to obtain diaphanous and homogenous electrolyte for electrodeposition. After that, the structures of 12CU, 12CU-$SnCl_2$ (0.1 M)-$CoCl_2$ (0.04 M)-$NiCl_2$ (0.04 M) and 12CU-$SnCl_2$ (0.1 M)-$CoCl_2$ (0.04 M)-$ZnCl_2$ (0.04 M) were characterized by spectroscopy (FTIR, AVATAR 370).

2.2 Electrochemical test

The electrochemical experiments were carried out on an AUTOLAB (PGSTAT30) electrochemical workstation completely. About 30 mL of the prepared 12CU, 12CU-$SnCl_2$ (0.1 M), 12CU-$CoCl_2$ (0.04 M), 12CU-$SnCl_2$ (0.1 M)-$CoCl_2$ (0.04 M), 12CU-$NiCl_2$ (0.04 M), 12CU-$SnCl_2$ (0.1 M)-$CoCl_2$ (0.04 M)-$NiCl_2$ (0.04 M), 12CU-$ZnCl_2$ (0.04 M) and 12CU-$SnCl_2$ (0.1 M)-$CoCl_2$ (0.04 M)-$ZnCl_2$ (0.04 M) were employed as electrolyte for cyclic voltammetry (CV) experiments. Meanwhile, about 30 mL electrolytes of 12CU-$SnCl_2$ (0.1 M)-$CoCl_2$ (0.04 M), 12CU-$SnCl_2$ (0.1 M)-$CoCl_2$ (0.04 M)-$NiCl_2$ (0.04 M) and 12CU-$SnCl_2$ (0.1 M)-$CoCl_2$ (0.04 M)-$ZnCl_2$ (0.04 M) were employed as electrolyte for chronomaperometry (CA) experiments.

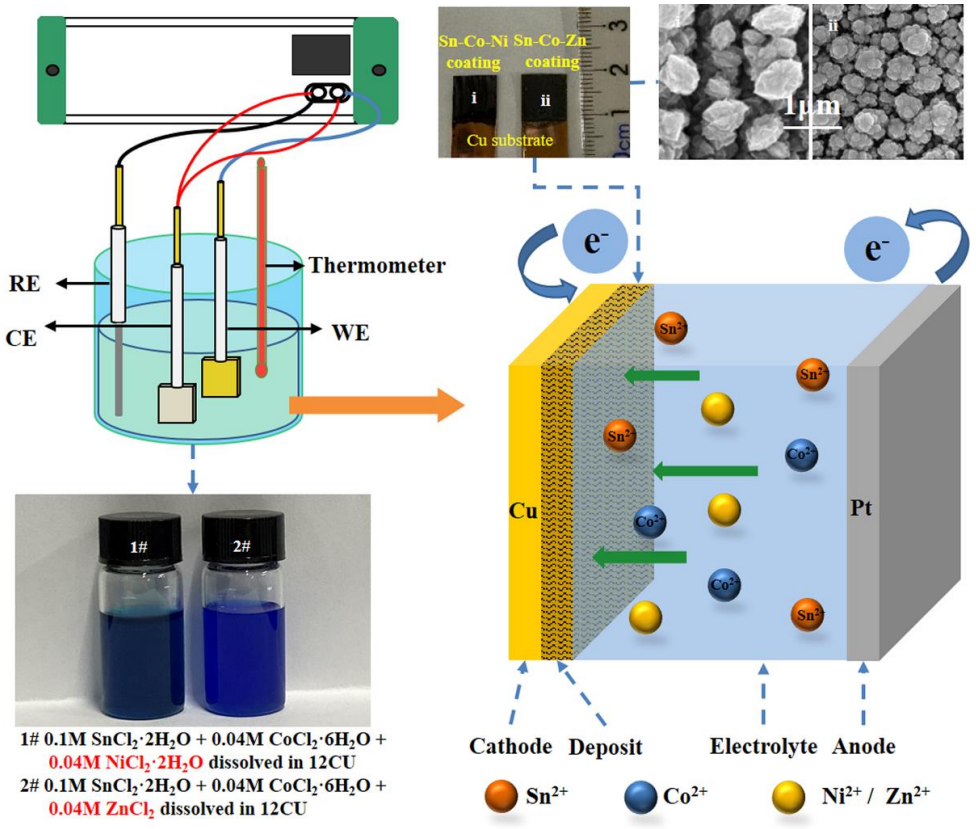

Figure 1. Schematic illustration of the electrodeposition of Sn-Co, Sn-Co-Ni and Sn-Co-Zn alloy coatings on Cu substrates from 12CU-$SnCl_2$ (0.1M)-$CoCl_2$ (0.04M)-($NiCl_2$ / $ZnCl_2$) (0.04M)

A three-electrode system was applied in the experiments. All electrodes were produced in Tianjin, China. A platinum plate (10 mm × 10 mm) was severed as a counter electrode. And a sliver wire (1.0 mm in diameter) was severed as a reference electrode. A platinum wire (0.5 mm in diameter) was applied as a working electrode in CV experiments. While a copper substrate (10 mm × 10 mm) was severed as a working electrode in electrodeposition experiments. Before experiments, all electrodes were washed with 5% HCl and distilled water, then dried in the drying oven. All experiments (CVs and CAs) were performed at 333 K. And CV experiments were performed at a scan rate of 10 mV s^{-1}. The CA experiments were performed at –0.9 V, –1.0 V and –1.1 V. After the experiments, the electrodeposited samples were washed with distilled water and alcohol, and then rapidly dried. Fig. 1 shows the schematic illustration of the experimental process for the electrodeposition on Cu substrate. And conditions for preparation of samples electrodeposited at 333 K in 12 CU are shown in Table 1.

Table 1. Conditions for preparation of samples electrodeposited at 333 K in 12 CU.

Samples	Alloy	Potential (V)	Electrodeposition time (min)	Samples	Alloy	Potential (V)	Electrodeposition time (min)
S1	SnCoNi	–0.9	10	S10	SnCoZn	–0.9	10
S2	SnCoNi	–0.9	30	S11	SnCoZn	–0.9	30
S3	SnCoNi	–0.9	60	S12	SnCoZn	–0.9	60
S4	SnCoNi	–1.0	10	S13	SnCoZn	–1.0	10
S5	SnCoNi	–1.0	30	S14	SnCoZn	–1.0	30
S6	SnCoNi	–1.0	60	S15	SnCoZn	–1.0	60
S7	SnCoNi	–1.1	10	S16	SnCoZn	–1.1	10
S8	SnCoNi	–1.1	30	S17	SnCoZn	–1.1	30
S9	SnCoNi	–1.1	60	S18	SnCoZn	–1.1	60

2.3 Alloy coating characterization

The component analysis of the Sn-Co-Ni and Sn-Co-Zn alloy coatings was obtained by X-ray photoelectron spectroscopy (XPS, Thermo ESCALAB 250XI). The coatings for XPS were S6 and S15. The microstructure and chemical composition of the Sn-Co-Ni and Sn-Co-Zn alloy coatings obtained at different cathodic potentials and different electrodeposition times at 333 K were characterized by a scanning electron microscope (SEM, FEI Nova NanoSEM 450) fitted with an energy-dispersive spectrometer (EDS). Potentiodynamic polarization experiments were performed to investigate the corrosion resistance of the deposited alloy coatings (S3, S6, S9, S12, S15 and S18). A three-electrode system was applied in these experiments. And a 3.5 wt% NaCl aqueous solution (30 mL) was served as the electrolyte of the tests. A platinum plate (10 mm × 10 mm) was served as a counter electrode. The electrodeposited sample (10 mm × 10 mm) was applied as a working electrode. While a saturated calomel electrode (SCE) was used as a reference electrode. Before the polarization

experiments, the samples were dipped in 3.5 wt% NaCl aqueous solution for about 30 min until the open-circuit potential (OCP) keeps stable. Polarization experiments were performed at room temperature and with a scan rate of 1 mV s^{-1}, and the potential range is from –500 to +500 mV around the OCP. Tafel extrapolation method was used to calculate the corrosion potential (E_{corr}) and corrosion current density (j_{corr}).

3. RESULTS AND DISCUSSION

3.1 FTIR analysis

To investigate the dissolution processes of chloride precursors in 12CU DES, the FTIR measurements were carried out. Fig. 2 illustrates the FITR spectra of pure 12CU, 12CU-$SnCl_2$ (0.1 M)-$CoCl_2$ (0.04 M)-$NiCl_2$ (0.04 M) and 12CU-$SnCl_2$ (0.1 M)-$CoCl_2$ (0.04 M)-$ZnCl_2$ (0.04 M).

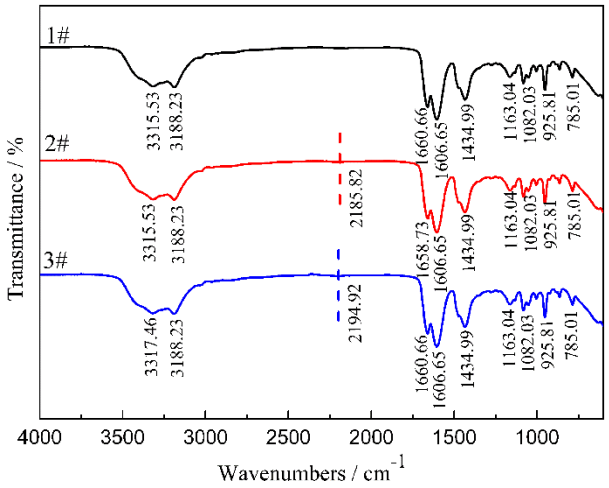

Figure 2. FTIR spectra of the DES solutions, 1# 12CU; 2# 12CU-$SnCl_2$ (0.1 M)-$CoCl_2$ (0.04 M)-$NiCl_2$ (0.04 M); and 3# 12CU-$SnCl_2$ (0.1 M)-$CoCl_2$ (0.04 M)-$ZnCl_2$ (0.04 M)

There are several peaks between 3000 and 3400 cm^{-1}, which demonstrates the existence of hydrogen bonds in the systems, where the hydrogen bonds are in the form of N-H…N-H, N-H…O-H, O-H…N-H and H-O…H-O [26]. The peaks nearby 1660 cm^{-1} are attributed to the hydrogen bonds in the form of C=O…H-O, and the peaks at 925.81 cm^{-1} suggest the presence of ν_{C-C} in the three systems, which suggests that the dissolving of metal salts cannot influence the structure of Ch^+. It should be noted that due to the different structures, the absorption peaks of the same groups have slight deviations [27]. The weak absorption peak at 2185.82 cm^{-1} (2#) is associated with the dissolution of metal salts in 12CU ionic liquid [28]. The similar phenomenon is also shown in 3#, and the absorption peak observed at 2194.93 cm^{-1}.

3.2 CV analysis

The results of CV analysis are illustrated in Fig. 3. Fig. 3a displays that the electrodeposition window of 12CU is from –0.86 V to 1.19 V. For the CV of 12CU-$SnCl_2 \cdot 2H_2O$ (0.1 M) in curve (i) of Fig. 3b, the reduction peak (c_1) at around –0.57 V and its corresponding oxidation peak (a_1) at about –0.24 V can be attributed to the deposition and oxidation processes of Sn(II)/Sn (Sn(II) + $2e^- \leftrightarrow$ Sn), respectively [29]. While, for the CV of the electrolyte only containing 0.04 M $CoCl_2 \cdot 6H_2O$ (curve (ii) in Fig. 3b), there is a reduction peak (c_2) at approximately –0.89 V, which is associated with the deposition of Co (Co(II) + $2e^- \rightarrow$ Co). And also an oxidation peak (a_2) at about –0.14 V is observed, which is owing to the stripping of Co deposits (Co – $2e^- \rightarrow$ Co(II)) [30]. It can be seen that the electrodeposition processes of Sn(II) and Co(II) are both one-step reduction processes in 12CU ionic liquid. Curve (iii) in Fig. 3b shows the CV of 12CU-$SnCl_2$ (0.1M)-$CoCl_2$ (0.04 M). The peak (c_3) at about –0.53 V is the reduction peak which can be attributed to the reduction of Sn (Sn (II) + $2e^- \rightarrow$ Sn), and the oxidation peak (a_3) at about –0.26 V is mainly attributed to the oxidation process of Sn (Sn – $2e^- \rightarrow$ Sn (II)). These observations indicate that the addition of Co(II) into the 12CU-$SnCl_2$ (0.1 M) makes little difference to the cathodic peak of Sn(II). While the reduction peak (c_4) and its corresponding oxidation peak (a_4) at –0.91 V and 0.25 V are attributed to the reduction and oxidation processes of Sn-Co alloys, respectively [31].

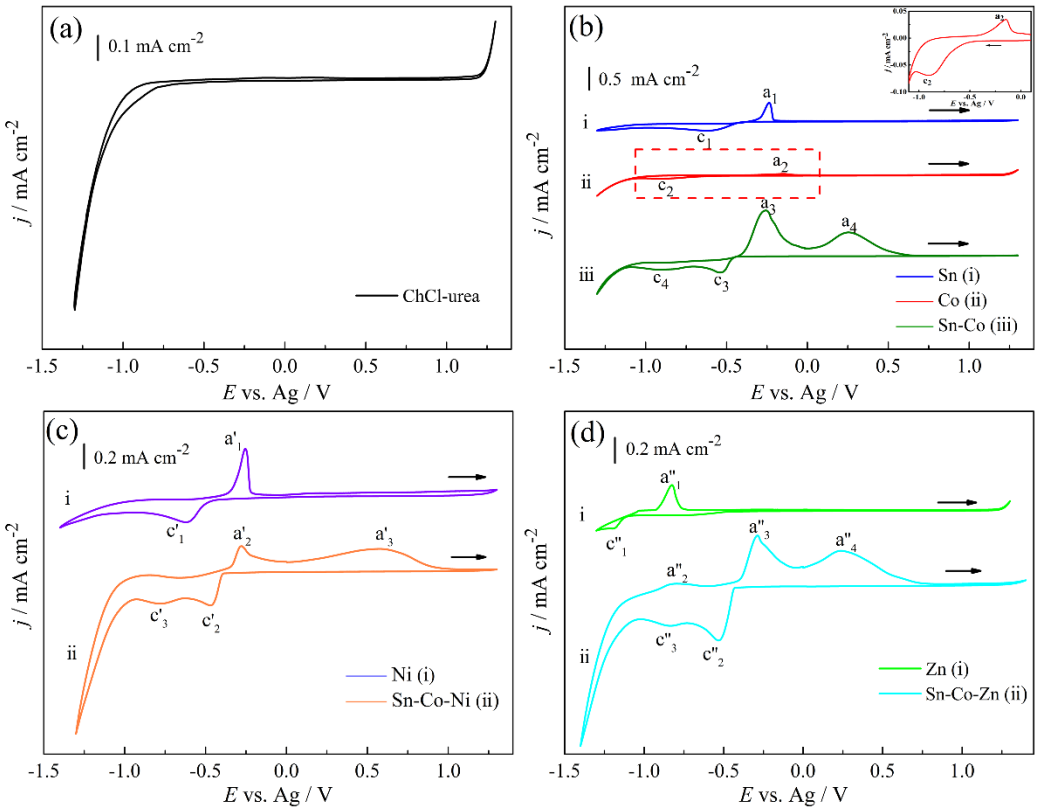

Figure 3. CV curves of a Pt working electrode at a scan rate of 10 mV s^{-1} in different electrolytes at 333 K, (a) 12CU; (b) i: 12CU-$SnCl_2$, ii: 12CU-$CoCl_2$, iii: 12CU-$SnCl_2$-$CoCl_2$, The inset is the enlarged part of the curve ii; (c) i: 12CU-$NiCl_2$, ii: 12CU-$SnCl_2$-$CoCl_2$-$NiCl_2$; (d) i: 12CU-$ZnCl_2$, ii: 12CU-$SnCl_2$-$CoCl_2$- $ZnCl_2$

Fig. 3c shows the CV of 12CU-$NiCl_2 \cdot 6H_2O$ (0.04 M) and 12CU-$SnCl_2$ (0.1 M)-$CoCl_2$ (0.04 M)-$NiCl_2$ (0.04 M). For the curve (i) in Fig. 3c, the reduction peak (c_1') at –0.62 V and its corresponding oxidation peak (a_1') at –0.25 V are attributed to the deposition and stripping processes of Ni(II) / Ni (Ni(II) + $2e^- \leftrightarrow$ Ni), respectively, which confirms the electrodeposition process of Ni (II) is also a one-step reduction process [32]. As is shown in Fig. 3c curve (ii), the cathodic reduction peak (c_2') at – 0.47 V and its corresponding oxidation peak (a_2') at –0.28 V are ascribed to the reduction processes and stripping of Sn(II)/Sn (Sn (II) + $2e^- \leftrightarrow$ Sn). The cathodic peak (c_3') around –0.77 V is associated with the reduction process of Co(II) (Co(II) + $2e^- \rightarrow$ Co) and Ni(II) (Ni (II) + $2e^- \rightarrow$ Ni) [33]. The introduction of Ni(II) promotes the electrodeposition of Co(II), thus leading to the potential of reduction of Co(II) moving positively. While the oxidation peak (a_3') at –0.58 V is associated with the stripping of Co (Co – $2e^- \rightarrow$ Co (II)) and Ni (Ni – $2e^- \rightarrow$ Ni (II)), respectively.

Fig. 3d shows the CVs of 12CU-$ZnCl_2$ (0.04 M) and 12CU-$SnCl_2$ (0.1 M)-$CoCl_2$ (0.04 M)-$ZnCl_2$ (0.04 M). For the curve (i), the reduction peak (c_1'') at –1.2 V and its relevant oxidation peak (a_1'') around –0.82 V are attributed to the reduction and stripping processes of Zn(II)/Zn(Zn(II) + $2e^- \leftrightarrow$ Zn), respectively. It reveals that the reduction process of Zn (II) is also a simple one-step reaction process. Fig. 3d curve (ii) shows the CVs of 12CU-$SnCl_2$ (0.1 M)-$CoCl_2$ (0.04 M)-$ZnCl_2$ (0.04 M), the peak (c_2'') at –0.52 V is attributed to the reduction of Sn (Sn(II) + $2e^- \rightarrow$ Sn). However, there is only one cathodic peak observed from –0.7 V to –1.1 V. It may be resulted from that Co/Zn is co-deposited in the electrolyte [34]. The cathodic peak (c_3'') at –0.86 V means the deposition of Co(II) (Co(II) + $2e^- \rightarrow$ Co) and Zn(II) (Zn (II) + $2e^- \rightarrow$ Zn). While the oxidation peak (a_2'') around –0.85 V is associated with the oxidation of Zn (Zn – $2e^- \rightarrow$ Zn(II)), respectively. Meanwhile, the oxidation peak (a_3'') at –0.29 V is associated with the oxidation process of Sn (Sn – $2e^- \rightarrow$ Sn(II)). And the peak (a_4'') at –0.24 V is due to the stripping of Co (Co – $2e^- \rightarrow$ Co(II)), respectively. On the basis of thermodynamics, the oxidation potential is related to the stability of the material. It suggests that the Sn-Co-Zn alloy is more stable than pure Co deposited in 12CU.

3.3 Chronoamperometric investigations

The chronoamperometric (CA) tests were carried out at different cathodic potentials to study the electrodeposition processes of Sn-Co, Sn-Co-Ni and Sn-Co-Zn alloy coatings in 12CU DES at 333 K on a Cu substrate. Current-time curves of Sn-Co alloy are shown in Fig.4a. Obviously, the current density decreases with time at the beginning of the electrodeposition. Then after a short time the current density reaches a platform, and finally comes to a stable value.

This observation illustrates that the uniform electrodeposits can be obtained. And with the increase of potential, the current density increases gradually. Fig. 4b displays the electrodeposition processes of Sn-Co-Ni alloy at potentials of –0.9 V, –1.0 V and –1.1 V. With the increase of time, the current density decreases at first, then it reaches a platform after a short time, and finally comes to a stable value, which suggests that the uniform electrodeposits can be obtained. For the electrodeposition processes of Sn-Co-Zn alloy at potentials of –0.9 V, –1.0 V and –1.1 V (in Fig. 4c), the phenomenon is similar to the electrodeposition of Sn-Co and Sn-Co-Ni alloys.

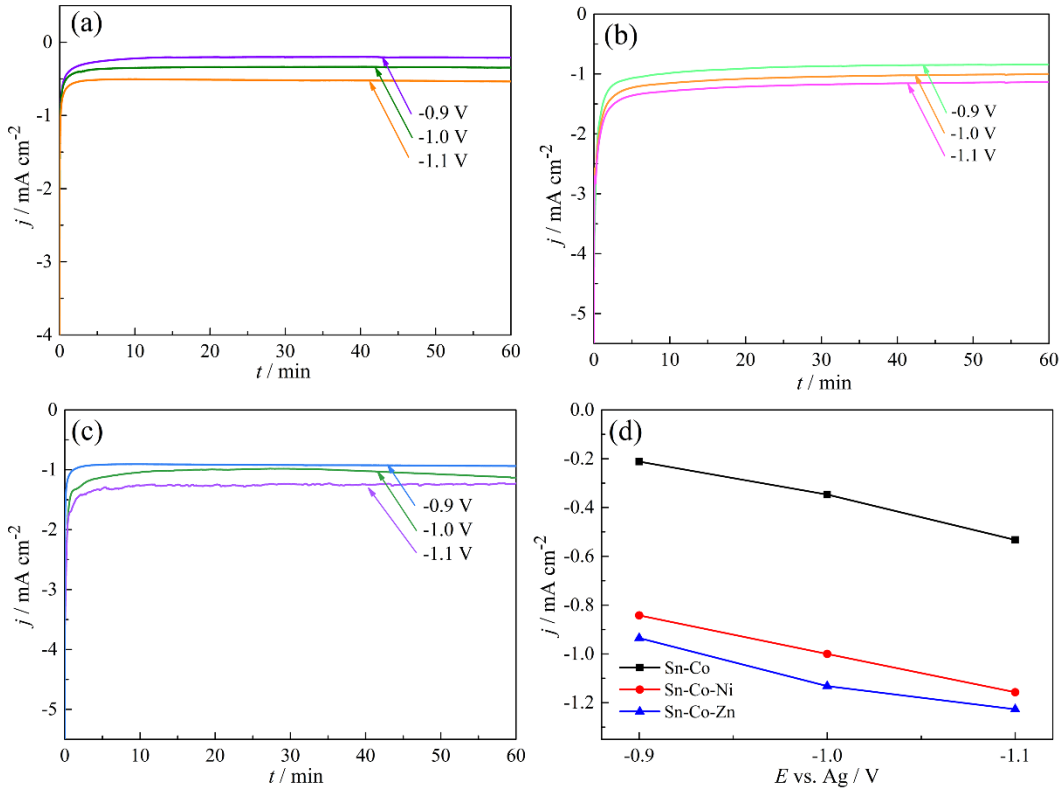

Figure 4. Current-time transient curves of the electrodeposition processes of alloy coatings on Cu substrates at different cathodic potentials and 333 K (a) Sn-Co alloy; (b)Sn-Co-Ni alloy; (c) Sn-Co-Zn alloy; (d) Relationships between average current density and cathodic potentials based on (a), (b)and (c)

In addition, Fig. 4d shows the relationship between current density and cathodic potentials. It can be seen that with the increase of applied cathodic potential, all of the current densities increase correspondingly. Comparing to Sn-Co alloy coating, the Sn-Co-Ni and Sn-Co-Zn alloy coatings both show a higher current density, which can be ascribed to the introduction of Ni(II) or Zn(II) into the electrolyte.

3.4 Characterization of the Sn-Co-Ni and Sn-Co-Zn alloy coatings

To investigate the chemical state of alloy coatings, XPS analysis of S6 and S15 is illustrated in Fig. 5(a-c) and Fig. 5(d-f). The Sn 3d peaks shown in Fig. 5a, two doublets are consisted of Sn $3d_{5/2}$ and Sn $3d_{3/2}$. The peaks located at 494.6 eV and 486.2 eV are attributed to the presence of Sn(IV). While the peaks at 493.8 eV and 485.4 eV are consistent with the metallic state Sn [35]. As shown in Fig. 5b, the peaks located at 796.1 eV and 780.7 eV can be associated with the Co $2p_{1/2}$ and Co $2p_{3/2}$, indicating the existence of Co(II). The peaks appeared at 802.4 eV and 785.9 eV are the satellite peaks of Co(II), further confirming the presence of Co(II) species [36,37]. Fig. 5c illustrates the Ni 2p spectrum, binding energies appeared at 872.8 and 855.5 eV, which are correspond to the Ni $2p_{1/2}$ and Ni $2p_{3/2}$. It demonstrates the existence of Ni(II). The satellite peaks of Ni(II) are located at 879.1 eV

and 861.6 eV. And the peaks appeared at 869.1 eV and 851.9 eV can be attributed to metallic nickel [38-40]. These results above can demonstrate that the Sn-Co-Ni alloy coating has been successfully electrodeposited. In Fig. 5d, the peaks at 494.4 eV and 486.0 eV are the Sn $3d_{5/2}$ and Sn $3d_{3/2}$, which can confirm the formation of Sn(IV) [41]. However, the peaks which can confirm the metallic state Sn did not appear.

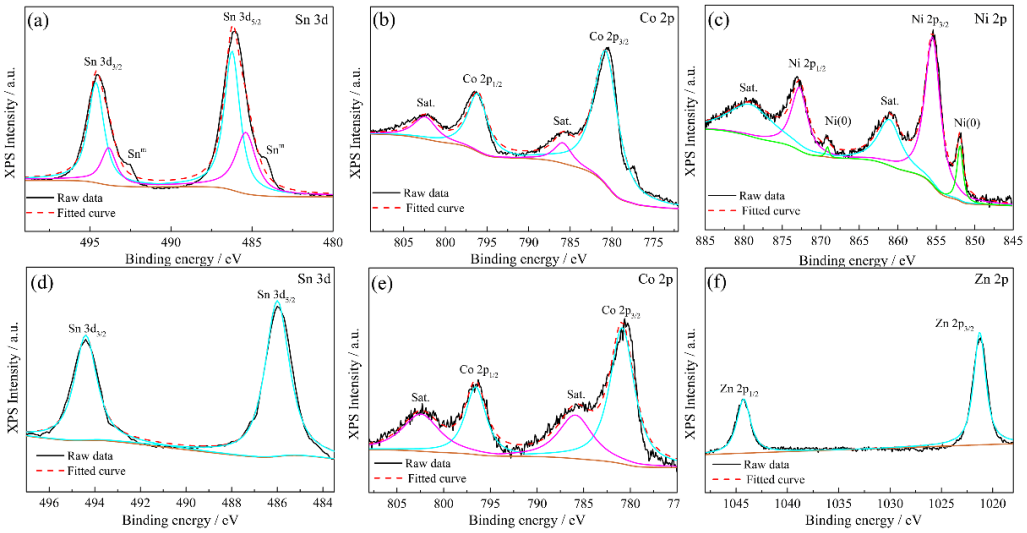

Figure 5. XPS spectra of alloy coatings, sample S6: (a) Sn 3d region; (b) Co 2p region; (c) Ni 2p region; sample S15: (d) Sn 3d region; (e) Co 2p region; (f) Zn 2p region

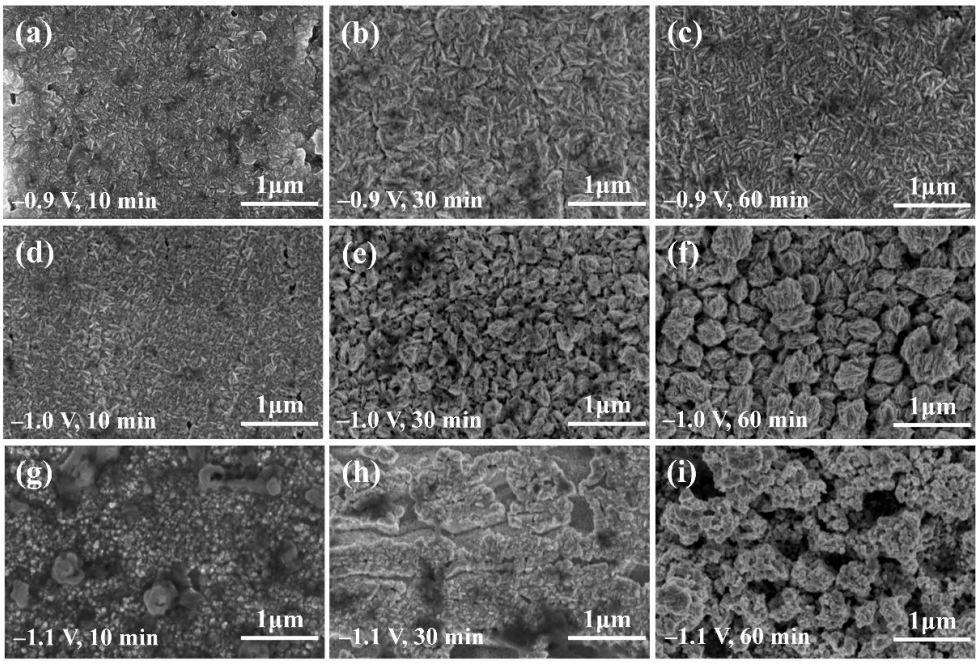

Figure 6. SEM images of the Sn-Co-Ni alloy coatings obtained in ChCl-urea at 333 K and different cathodic potentials for different electrodeposition times on Cu substrate

Fig. 5e shows that, the peaks Co $2p_{1/2}$ and Co $2p_{3/2}$ appear at 796.5 eV and 780.87 eV, and the peaks located at 802.4 eV and 785.9 eV can demonstrate the existence of Co(II) species [42]. As

shown in Fig. 5f, the Zn $2p_{1/2}$ and Zn $2p_{3/2}$ at 1044.3 eV and 1021.3 eV are attributed to the presence of Zn(II) [43,44]. These results can prove that Sn-Co-Zn alloy coating has also been prepared successfully.

Fig. 6 displays the morphologies of the Sn-Co-Ni alloy coatings obtained in ChCl-urea DES at 333 K and different cathodic potentials for different electrodeposition times. For Fig. 6 (a-c), the coatings are S1, S2 and S3. When the electrodeposition was carried out at –0.9 V for different times, uniform structure and needle-like crystals can be observed on the coating surface. With the increase of electrodeposition time, the needle-like crystals grow up to form flaky particles. The SEM images of Sn-Co-Ni alloy coatings (S4, S5, S6) can been seen in Fig. 6(d-f). These morphologies also appear the shape of needle, and then the particles gradually grow up to form a three-dimensional structure along with the increase of electrodeposition time at –1.0 V and 333 K. Fig. 6(g-i) show the SEM images of S7, S8 and S9. It can be observed that the surface of the coatings becomes rough and uneven. The agglomerates have been formed in these coatings. The hollow structure has been obtained at –1.1 V for 60 min. With the increase of potential, particles convert from needle-like crystals to three-dimensional structure. With the further increase of potential, structure becomes agglomerates. In the paper [45], the film Sn-Co-Ni alloy coatings were obtained by electroplating on Cu foil, which shows the rod-like structure and smooth uniform surface. It can be seen that different morphology of SnCoNi alloy can be obtained by different methods.

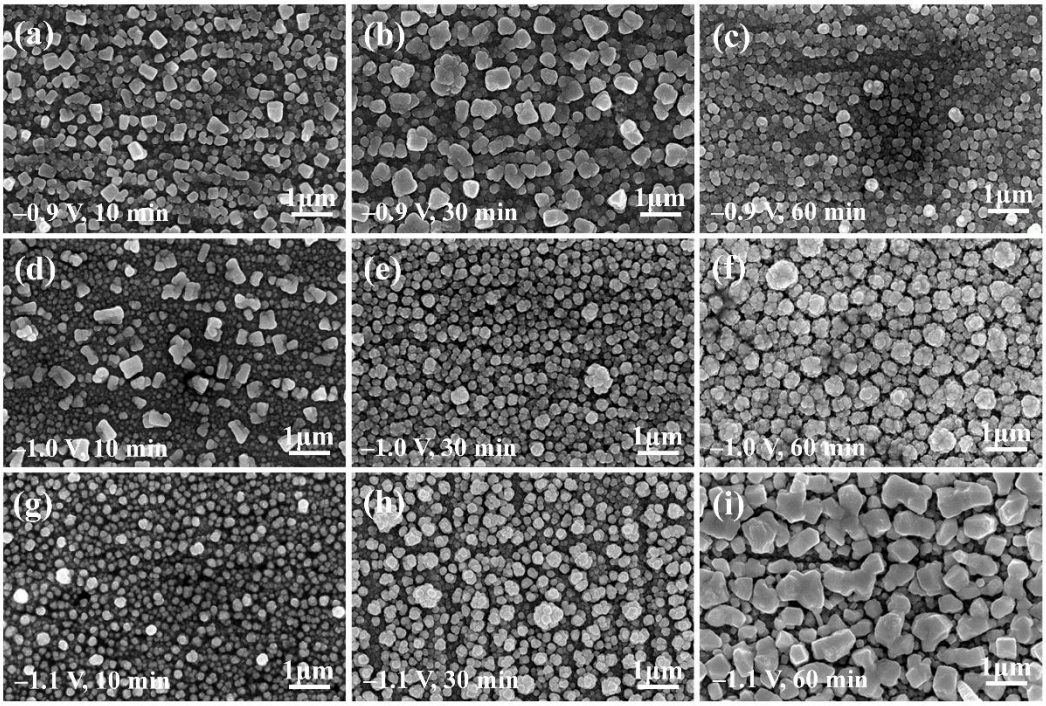

Figure 7. SEM images of the Sn-Co-Zn alloy coatings obtained in ChCl-urea DES at 333 K and at different cathodic potentials for different electrodeposition times

The morphologies of the Sn-Co-Zn alloy coatings obtained in 12CU at 333 K and at different cathodic potentials for different electrodeposition times are illustrated in Fig. 7. The SEM images of Sn-Co-Zn coatings (S10, S11, S12) can been seen in Fig. 7(a-c). When the electrodeposition was

performed at the potential of –0.9 V for 10 min, uniform structure and cubic crystals can be obviously observed on the coating surface.

With the increase of electrodeposition time, the cubic crystals grow up to form flower-shape particles, and the particles become denser. Fig. 7(d-f) show SEM images of S13, S14 and S15. Obviously, with the increase of time, the cubic crystals grow up to form flower-shape particles. Fig. 7(g-i) show the alloy coatings (S16, S17, S18). At the potential of –1.1 V for 10 min, flower-shape particles can be obviously observed on the coating surface. With the increase of electrodeposition time, particle becomes lager and denser. And also, with the increase of potential, particles transform from cubic crystals to flower-shape particles. With the further increase of cathodic potential, structure becomes agglomerates. The Sn-Co-Zn alloy coatings show the smooth and flat surface with few cracks in the organic solvent [46]. The Sn-Co-Zn alloy coatings electrodeposited on Cu nanorods array presents nanorods array with particles distributed on the surface [47]. It is suggested that SnCoZn alloy electrodeposited in different electrolytes or on different substrates would have different morphologies.

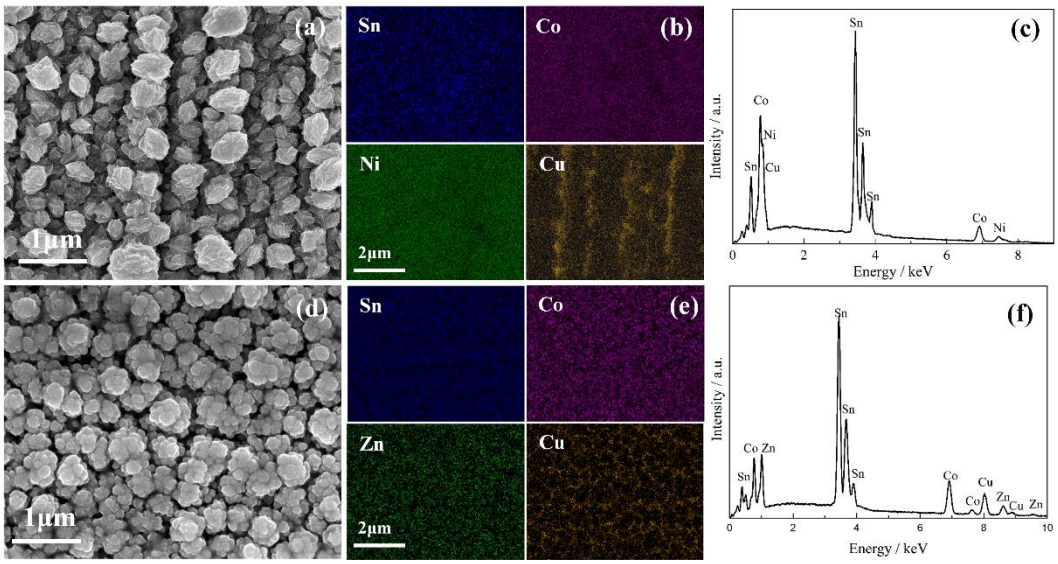

Figure 8. (a) SEM images of S6; (b) EDS elemental mapping of (a) containing elements Sn, Co, Ni and Cu; (c) EDS spectrum measured over the imaging area (a); (d) SEM image of S15; (e) EDS elemental mapping of (d) containing elements Sn, Co, Zn and Cu; (f) EDS spectrum measured over the imaging area (d)

The SEM image and EDS spectrum of S6 are displayed in Fig. 8(a-c). While Fig. 8(d-f) show the SEM image and EDS spectrum of S15. In Fig. 8b, the EDS elemental mappings evidence the uniform distribution of Sn, Co, and Ni. The corresponding EDS spectrum shown in Fig. 8c displays that the Sn-Co-Ni alloy coating contains 38.35 at.% Sn, 34.14 at.% Co and 27.51 at.% Ni. The unmarked peak belongs to O element, which is caused by slight oxidation of the alloy coating. This observation demonstrates that the Sn-Co-Ni alloy coating has been successfully electrodeposited. Fig. 8d displays the SEM image of S15. In Fig. 8e, the EDS elemental mappings evidence the distribution of elements Sn, Co, Zn and Cu is uniform. The EDS spectrum of the obtained Sn-Co-Zn alloy coating reveals that the electrodeposits contain 45.26 at.% Sn, 33.49 at.% Co and 21.25 at.% Zn elements, as

shown in Fig. 8f. This observation suggests that the Sn-Co-Zn coating has been successfully electrodeposited.

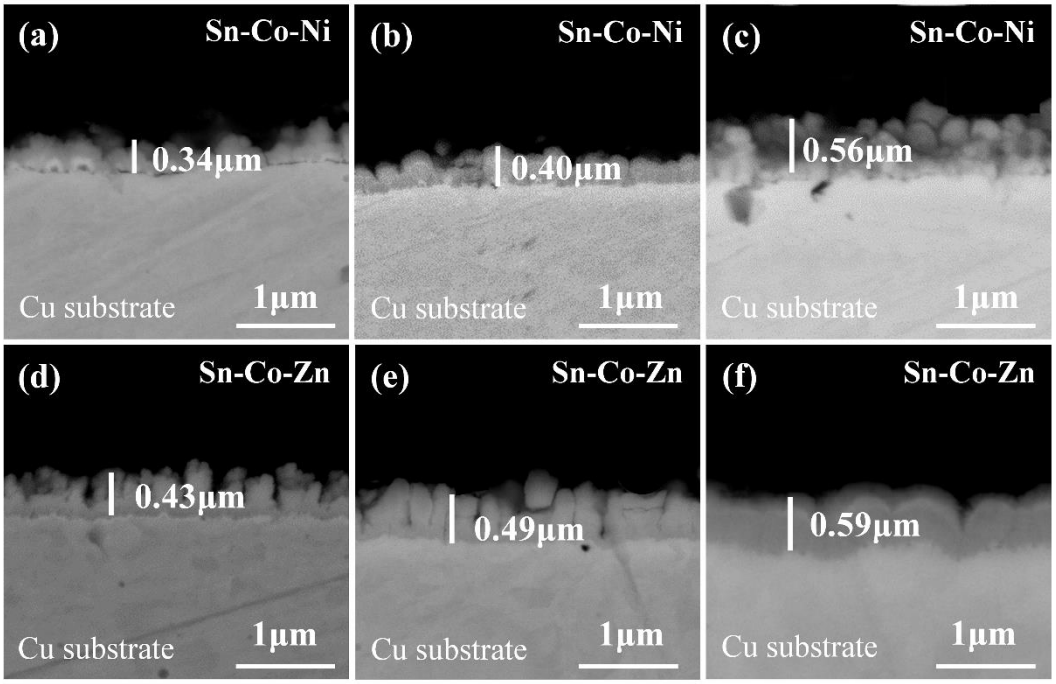

Figure 9. Cross-sectional SEM images of alloy coatings: (a) S3; (b) S6; (c) S9; (d) S12; (e) S15; (f) S18

Fig. 9(a-c) illustrates the cross-sectional morphologies of the Sn-Co-Ni alloy coatings obtained at different potentials in 12CU. It can be seen that, with the increase of negative potential, the thickness of these coatings generally increases. The average thickness of the Sn-Co-Ni coatings is approximately 0.4 μm. We note that the thickness of the alloy coating can be controlled by changing the electrodeposition time. Fig. 9(d-f) show that the cross-sectional morphologies of the Sn-Co-Zn alloy coatings obtained at different cathodic potentials. It can be seen that, with the increase of potential, the thickness of these alloy coatings also generally increases. The average thickness of the Sn-Co-Zn coatings is approximately 0.5 μm. The Sn-Co-Zn alloy coating is thicker than the Sn-Co-Ni alloy coating obtained under the same electrodeposition condition.

3.5 Corrosion-resistance performance of the Sn-Co-Ni and Sn-Co-Zn alloy coatings

To research the corrosion-resistance performance of the Sn-Co-Ni and Sn-Co-Zn alloy coatings, the polarization experiments were carried out in 3.5 wt% NaCl at room temperature. Fig. 10 shows the potentiodynamic polarization curves of the Cu substrate and deposited Sn-Co-Ni and Sn-Co-Zn alloy coating.

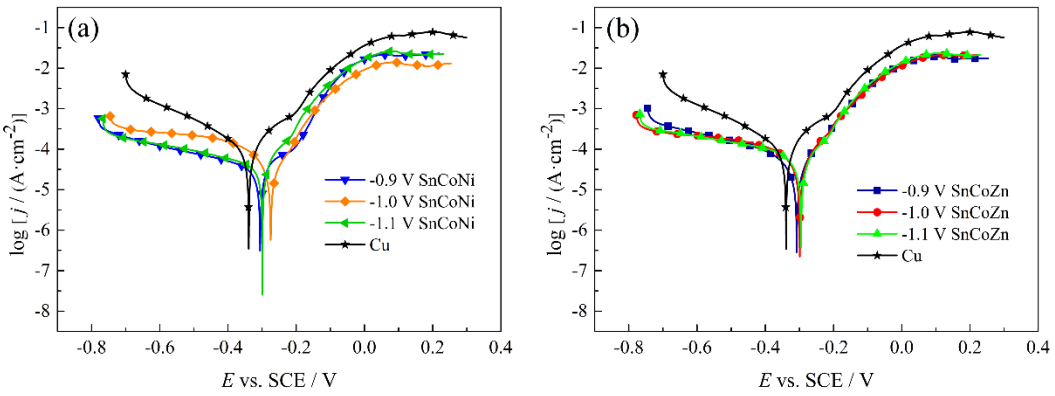

Figure 10. Potentiodynamic polarization curves of the Cu substrate and (a) Sn-Co-Ni and (b) Sn-Co-Zn alloy coatings deposited at different potentials and room temperature in 3.5 wt% NaCl solution

The Sn-Co-Ni and Sn-Co-Zn alloy coatings are electrodeposited at 333 K and different potentials for 60 min in 12CU DESs. The corrosion behaviors containing corrosion current density (j_{corr}) and corrosion potential (E_{corr}) obtained from Tafel extrapolation are shown Table 2.

Table 2. Corrosion characteristics of the Cu substrate and the Sn-Co-Ni and Sn-Co-Zn alloy coatings deposited at different potentials and room temperature in 3.5 wt% NaCl solution.

Samples	j_{corr} (μA cm^{-2})	E_{corr} (V)
S3	55.0	–0.306
S6	48.0	–0.275
S9	56.1	–0.299
S12	43.9	–0.308
S15	67.2	–0.229
S18	49.4	–0.295
Cu	129.9	-0.337

In Fig. 10a, with the potential increases from –0.9 V to –1.1 V, E_{corr} of Sn-Co-Ni coating firstly increases and then decreases, while j_{corr} firstly decreases and then rises. The S2 shows the best corrosion resistance, which can be owing to its dense morphology and a three-dimensional structure (in Fig. 6f). In Fig. 10b, similar corrosion behavior can be seen in the Sn-Co-Zn alloy coatings achieved at different potentials. Because of its dense morphology, S4 shows the lower j_{corr} than S5 and S6. With the increase of potential, the morphology becomes looser (in Fig. 7f and Fig. 7i), and Cl^- is easier to contact with substrate, which increases the rate of corrosion. It can be seen that Sn-Co-Ni coatings generally present the better corrosion resistance than Sn-Co-Zn coatings. Because Ni has a good corrosion resistance, the existence of Ni improves the performance of Sn-Co-Ni coatings.

4. CONCLUSIONS

In this work, Sn-Co, Sn-Co-Ni and Sn-Co-Zn alloys have been prepared by electrodeposition in 12CU-$SnCl_2$ (0.1 M)-$CoCl_2$ (0.04 M), 12CU-$SnCl_2$ (0.1 M)-$CoCl_2$ (0.04 M)-$NiCl_2$ (0.04 M) and 12CU-$SnCl_2$ (0.1 M)-$CoCl_2$ (0.04 M)-$ZnCl_2$ (0.04 M). The electrodeposition processes have been investigated, and the obtained products have been characterized and compared. The results prove that the potential has important influences on the electrodeposition and the microstructures of the alloy coatings. With the increase of potential, morphology of the Sn-Co-Ni alloy coating grows from needle-like crystals to three-dimensional structure. In contrast, with the increase of potential, the morphology of the Sn-Co-Zn alloy coating grows from cubic crystals to flower-shape particles. Meanwhile, the electrodeposition time can also influence the microstructure of the Sn-Co-Ni and Sn-Co-Zn alloy coatings. And the Sn-Co-Ni coating obtained at –1.0 V at 333 K for 60 min presents the best corrosion resistance due to its dense morphology. In addition, the corrosion-resistance performances of Sn-Co-Zn alloy coatings electrodeposited at different potentials are similar. These results suggest that the electrodeposition of Sn-Co-Ni and Sn-Co-Zn alloys in ChCl-urea DES is a simple and controllable process.

ACKNOWLEDGEMENTS
This work was financially sponsored by the National Natural Science Foundation of China (Nos. 51974181; 51574164), the Shanghai Rising-Star Program (19QA1403600), and the Iron and Steel Joint Research Found of National Natural Science Foundation and China Baowu Steel Group Corporation Limited (U1860203), the authors also thank the Program for Professor of Special Appointment (Eastern Scholar) at Shanghai Institutions of Higher Learning (TP2019041) and the CAS Interdisciplinary Innovation Team for financial support.

References

1. F. Khatkhatay, L. Jiao, J. Jian, W. Zhang, Z. Jiao, J. Gan, H. Zhang, X. Zhang and H. Wang, *J. Nucl. Mater.*, 451 (2014) 346.
2. S. Rao, X. Zou, S. Wang, T. Shi, Y. Lu, L. Ji, H. Hsu, Q. Xu and X. Lu, *J. Electrochem. Soc.*, 166 (2019) 427.
3. M. Winnicki, A. Baszczuk, M. Rutkowska-Gorczyca, A. Małachowska and A. Ambroziak, *Surf. Eng.*, 32 (2016) 691.
4. Z. Mao, J. Ma, J. Wang and B. Sun, *Appl. Surf. Sci.*, 255 (2009) 3784.
5. Z. Hu, X. Jie, and G. Lu, *J. Coat. Techol. Res.*, 7 (2010) 809.
6. S. Alex, B. Basu, S. Sengupta, U. Pandey and K. Chattopadhyay, *Appl. Therm. Eng.*, 109 (2016) 1003.
7. M. Esfahani, J. Zhang, Y. Wong, Y. Durandet and J. Wang, *J. Electroanal. Chem.*, 813 (2018)143.
8. H. Kazimierczak, P. Ozga, A. Jałowiec and R. Kowalik, *Surf. Coat. Tech.*, 240 (2014) 311.
9. C. Meudre, L. Ricq, J. Hihn, V. Moutarlier, A. Monnin and O. Heintz, *Surf. Coat. Tech.*, 252 (2014) 93.
10. P. Huang and Y. Zhang, *Int. J. Electrochem. Sci.*, 13 (2018) 10798.
11. F. Liu, Y. Deng, X. Han, W. Hu and C. Zhong, *J. Alloy Compd.*, 654 (2016) 163.
12. C. Verma, E. Ebenso and M. Quraishi, *J. Mol. Liq.*, 233 (2017) 403.
13. J. Zhang, X. Ma, J. Zhang, P. Yang, M. An and Q. Li, *J. Alloy Compd.*, 806 (2019) 79.

14. Y. Hou, R. Li, J. Liang, P. Su and P. Ju, *Surf. Coat. Tech.*, 335 (2018) 72.
15. L. Wang, G. Chen, Q. Shen, G. Li, S. Guan and B. Li, *Int. J. Min. Met. Mater.*, 25 (2018) 1027.
16. J. Sun, T. Ming, H. Qian and Q. Li, *Electrochim. Acta*, 297 (2019) 87.
17. J. Li, H. Zhu, C. Peng and H. Liu, *J. Mol. Liq.*, 284 (2019) 675.
18. W. Freyland, C. Zell, S. El Abedin and F. Endres, *Electrochim. Acta*, 48 (2003) 3053.
19. A. Abbott, D. Boothby, G. Capper, D. Davies and R. Rasheed, *J. Am. Chem. Soc.*, 126 (2004) 9142.
20. H. F. Alesary, A. F. Khudhair, S. Y. Rfaish, and H. K. Ismail, *Int. J. Electrochem. Sci.*, 14 (2019) 7116.
21. W. Chiang, J. Huang, P. Chen, P. Wu, A. Joi and Y. Dordi, *J. Alloy Compd.*, 742 (2018) 38.
22. J. Zhong, L. Li, M. Waqas, X. Wang, Y. Fan, J. Qi and S. Sun, *Electrochim. Acta*, 322 (2019) 134677.
23. G. Thorat, H. Jadhav, W. Chung and J. Seo, *J. Alloy Compd.*, 732 (2018) 694.
24. S. Salomé, N. Pereira, E. Ferreira, C. Pereira and A. Silva, *J. Electroanal. Chem.*, 703 (2013) 80.
25. L. Anicai, A. Petica, S. Costovici, P. Prioteasa and T. Visan, *Electrochim. Acta*, 114 (2013) 868.
26. D. Yue, Y. Jia, Y. Yao, J. Sun and Y. Jing, *Electrochim. Acta*, 65 (2012) 30.
27. H. Wang, Y. Jing, X. Wang, Y. Yao and Y. Jia, *J. Mol. Liq.*, 170 (2012) 20.
28. X. Xie, X. Zou, X. Lu, K. Zheng, H. Cheng, Q. Xu and Z. Zhou, *J Electrochem. Soc.*, 163 (2016) 537.
29. L. Bengoa, P. Pary, M. Conconi and W. Egli, *Electrochim. Acta*, 256 (2017) 211.
30. R. Critelli, P. Sumodjo, M. Bertotti and R. Torresi, *Electrochim. Acta*, 260 (2018) 762.
31. J. Zhang, C. Gu, S. Fashu, Y. Tong, M. Huang, X. Wang and J. Tua, *J. Electrochem. Soc.*, 162 (2015)1.
32. S. Wang, X. Zou, Y. Lu, S. Rao, X. Xie, Z. Pang, X. Lu, Q. Xu and Z. Zhou, *Int. J. Hydrogen Energ.*, 43 (2018) 15673.
33. W. Li, J. Hao, S. Mu and W. Liu, *Appl. Surf. Sci.*, 507 (2020) 144889.
34. Q. Chu, J. Liang and J. Hao, *Electrochim. Acta*, 115 (2014) 499.
35. S. Xia, L. Yao, H. Guo, X. Shen, J. Liu, F. Cheng and J. Liu, Guo H et al. *J. Power Source*s, 440 (2019) 227162.
36. J. Yin, Z. Li, Y. Yu, Y. Lv, K. Song, B. Yang and X. Hu, *Ceram. Int.*, 45 (2019) 13401.
37. J. Feng, H. Wang, Z. Hu, M. Zhang, X. Yang, R. Yuan and Y. Chai, *Ceram. Int*., 45 (2019) 13369.
38. W. Dai, L. Lin, Y. Li, F. Li and L. Chen, *Int. J. Hydrogen Energ.*, 44(2019) 28746.
39. D. Li, B. Li, S. Du and W. Zhang, *Ceram. Int.*, 45 (2019) 24884.
40. B. Yuan, F. Sun, C. Li, W. Huang and Y. Lin, *Electrochim. Acta*, 313 (2019) 91.
41. M. Salleh, S. McDonald, Y. Terada, H. Yasuda and K. Nogita, *Mater. Design*, 82 (2015) 136.
42. H. Zhang, P. Dong, Y. Ni and J. Gao, *Mater. Charact.*, 132 (2017) 422.
43. Q. Du, D. Wei, S. Liu, S. Cheng, N. Hu, Y. Wang, B. Li, D. Jia and Y. Zhou, *Surf. Coat. Tech.*, 352 (2018) 489.
44. D. Cabrera-German, G. Molar-Velázquez, G. Gómez-Sosa, W. De la Cruz and A. Herrera-Gomez, *Surf. Interface Anal.*, 49 (2017) 1078.
45. R. Gnanamuthu and C. Lee, *Mater. Sci. Eng. B-Adv.*, 176 (2011) 1329.
46. Y. Chang, L. Huang and S. Sun, *Acta Phys-Chim Sin*, 26 (2010) 561.
47. Y. Chang, N. Wang, X. Li, and L. Huang, *battery bimonthly,* 45 (2015) 26.